Research Article

Oxidation of electroless Ni–P coated AISI 430 alloy and effect of pre-reduction

Mark K. King Jr.[1] · **Manoj K. Mahapatra**[1]

Received: 31 January 2020 / Accepted: 16 March 2020 / Published online: 19 March 2020

Abstract

The oxidation behavior of electroless Ni–P coated AISI 430 alloy was investigated at 800 °C in moisture-saturated (~ 3% H_2O) air. Effect of pre-reduction in dry hydrogen (Ar-3%H_2) at 800 °C on the oxidation behavior of the Ni–P coated AISI 430 was also studied. Microstructure, chemical composition, and compound/oxide phase formation across the oxide layer were analyzed by scanning electron microscopy, energy dispersive spectroscopy, and X-ray diffraction techniques. Iron oxide Fe_2NiO_4 spinel along with other oxide and spinel phases are found in the multilayered oxide scale for both the Ni–P coated and pre-reduced Ni–P coated AISI 430 alloy. Ni–P coating crystallization and oxidation initiates the oxidation for the electroless sample. Ni_3P and $FeNi_3$ intermetallic compounds formed during reduction initiates the oxidation of the pre-reduced sample.

Keywords Ni–P coating · Oxidation · Pre-reduction · Spinel · Iron oxide

1 Introduction

Coatings on various surfaces are common to improve corrosion and wear resistance, and functional properties. The performance of a coating primarily depends on its composition, adherence with the substrate, chemical stability, and compatibility and mechanical integrity with the substrate in application environment. Nickel coating finds wide range of applications for its excellent corrosion resistance, tribological properties, and functional properties. Electroless deposition, an autocatalytic method, of nickel has penetrated into wide array of commercial and niche markets [1, 2] ranging from engineering tools, offshore wind turbine [3], aerospace [4], and heat exchangers in petroleum industries [5] to solar absorbers for space applications [6].

Common reductants such as sodium hypophosphite, sodium borohydride, or hydrazine are added in the bath for electroless nickel deposition, which form Ni–P, Ni–B, or Ni coatings, respectively [7]. Ni–P coating has been extensively investigated. Increasing P-content increases the corrosion resistance and electrical resistivity [8, 9]. Increase in P content up to ~ 8 at% increases the hardness and wear resistance of the coating [10, 11].

The high temperature properties of electroless nickel coating has also been studied. The hardness of Ni–P coating increases up to 400 °C due to precipitation of crystalline Ni_3P, Ni_5P_2, and $Ni_{12}P_5$ phases [2]. Electrical resistivity and non-magnetic property also improves [12, 13]. Nickel coating has been investigated to decrease electrical resistance of chromia forming ferritic steel, the metallic interconnect, for high temperature (650–800 °C) solid oxide fuel cell (SOFC) application [14]. Nickel coating decreases chromium vaporization from the ferritic steel [14, 15]. Nickel oxide and spinel at the oxide surface attributes to these effects. These studies do not provide oxidation

---

Mark K. King and Manoj K. Mahapatra have equally contributed.

✉ Manoj K. Mahapatra, mkmanoj@uab.edu | [1]Department of Materials Science and Engineering, University of Alabama at Birmingham, Alabama, USA.

SN Applied Sciences (2020) 2:716 | https://doi.org/10.1007/s42452-020-2556-z

mechanism of nickel coated ferritic steel although inform about the oxide phases at the surface and interfaces.

Ni–P coating interaction with metallic substrates is also studied [16–19]. $FeNi_3$ intermetallic layer formation due to nickel diffusion into a carbon steel followed by a Ni_3P layer and outward diffusion of phosphorous from the coating/steel interface are reported both for Ni–P coated steel annealed at 800 °C in air [16] and at 650 °C in argon [18]. Formation of NiO at 607 °C and Fe_xNi_yO at ≥ 695 °C is reported for a Ni–P coated iron annealed in air [17] while the other study does not report any oxide [16]. Iron diffusion from steel and subsequent formation of Fe_2O_3 and $(Fe,Ni)_3O_4$ has been reported due to oxidation of Ni–P coated steel substrate [19]. All these studies show that phosphorous does not participate in forming oxides; indeed, it may provide a diffusion barrier layer. It is worthy to investigate further the role of Ni–P layer on oxidation of chromia forming ferritic steel—the aim of our study.

We have investigated the oxidation of an electroless Ni–P coated AISI 430 isothermally at 800 °C in moisture saturated (~ 3% H_2O) air for 100 h. The composition of AISI 430 is similar, if not identical, to the SOFC metallic interconnects as given in Table 1 [20]. Moisture saturated air replicates the SOFC cathode environment. We have also studied the oxidation of the Ni–P coated AISI 430 pre-reduced in Ar-3% H_2.

2 Materials and methods

2.54 cm × 2.54 cm × 0.06 cm AISI 430 coupons (MSC Industrial Supply Co. USA) were cleaned and nickel coated by a proprietary electroless deposition method (Advanced Technical Finishing, USA) in accordance to MIL-C-26074 Class 1. One set of the electroless nickel coated AISI 430 coupons were reduced at 800 °C for 2 h at 3 °C min^{-1} ramp rate in Ar-3% H_2 gas (certified) at 100- sccm flow rate. The reduced samples were designated as R-electroless.

The electroless and R-electroless samples were oxidized in a moisture saturated (~ 3% H_2O) flowing air (ultra-high purity, 100-sccm flow rate) at 800 °C for 10 h, 20 h, 50 h, and 100 h at 3 °C min^{-1} ramp rate in an atmosphere controlled furnace (Lindberg, Model 54233, Waterson, WI USA). Air was flown through deionized water at room temperature to be moisture-saturated. The photograph of the experimental set up is shown in Fig. 1. The oxidation time was cumulative. Therefore, the samples oxidized for 100 h experienced four thermal cycles. The oxidized samples were weighed using an analytical balance (Mettler Toledo, Model AG245, Switzerland) to determine the oxidation rate.

X-ray diffractometer (XRD) (Siemens D500, KRISTALLOFLEX DACO-MP 710/710 H)) was used to identify the crystalline compounds. The samples were scanned in

Table 1 Nominal compositions (wt%) of metallic interconnects for solid oxide fuel cell systems [20]

Interconnect	Fe	Cr	Mn	Ti	Si	Al	C	S	P	Ni	Nb	Re
Crofer 22 APU	76.59	22.80	0.45	0.08			0.005	0.002	0.016			0.06
AISI 441	80.68	17.60	0.33	0.18	0.47	0.045	0.01	0.001	0.024	0.20	0.46	–
AISI 430	82.36	16.94	0.57	–	0.13	–	–	–	–	–	–	–

AISI 430 composition is determined from EDS analysis

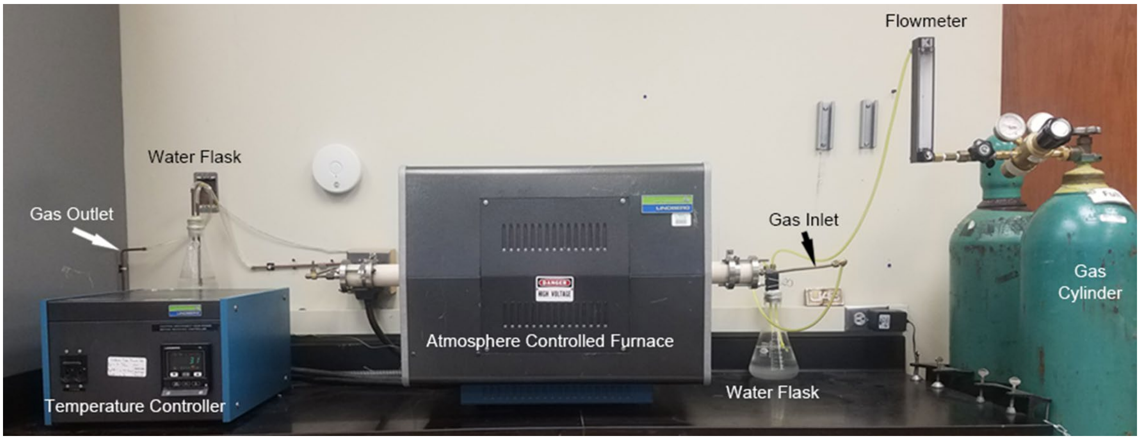

Fig. 1 Photograph of the experimental set-up for oxidation study

15–80° 2θ range with 0.04° step size using Cu Kα radiation ($\lambda = 1.5406$ Å) and Ni filter.

Scanning electron microscope (SEM) (FEI Quanta 650 FEG, USA) was used to analyze the surface morphology and interfacial microstructure of the as-received and oxidized samples. The R-electroless sample was coated with Ni–Cu topcoat and the oxidized samples were coated with a Ni topcoat to prevent the original coating and oxide layer from spallation during sample preparation for investigating interfacial microstructure. The cross-sections of samples were polished to optical finish. The elemental composition of the coated substrate and oxide layer was determined by energy dispersive spectrometer (EDS, AMETEK EDAX) attached to the SEM. The EDS spot analysis provides the compositional variation for different phases and/or layers although the spatial resolution (> 1 μm) and fluorescence effect limits the accuracy of the quantitative analysis [21]. The elemental compositions are reported in atomic percent (at%). EDS line scan profile was collected to obtain elemental distribution across the interface. Elemental mapping visually complements EDS spot and line scan analysis.

3 Results and discussion

3.1 Coating characteristics

The electroless coating is uniform as seen from the surface morphologies in Fig. 2a. The nickel coating is 5.24 ± 0.10 μm thick (Fig. 2b), adheres well with the AISI 430 substrate, and contains 18.4 ± 2.6 at% phosphorus as detected by SEM–EDS analysis. The XRD plot in Fig. 3 confirms that the electroless Ni–P coating is amorphous.

Surface morphology of the R-electroless sample in Fig. 4a shows that grains are surrounded by bright particles (~ 0.24 ± 0.02 μm). The appearance of the grains is similar to crystalline phases (0.37 ± 0.07 μm) in an amorphous matrix. The grains are enriched of nickel and phosphorous (46.6 ± 1.9 Ni, 12.2 ± 0.6 Fe, 22.4 ± 0.88 P, 0.6 ± 0.1 Cr, 0.2 ± 0.1 Mn, 18.1 ± 1.7 O). The bright particles at the grain boundaries contain 25.3 ± 6.7 Ni, 11.3 ± 1.1 Fe, 15.3 ± 2.2 P, 4.7 ± 2.9 Cr, 0.6 ± 0.4 Mn, 42.7 ± 6.6 O. Higher chromium and oxygen content at the grain boundaries than those in the grains suggests that the bright particles are Cr_2O_3. Pores (marked with dotted circle) are observed at the grain boundaries for two plausible reasons. Firstly, amorphous Ni–P coating crystallizes into Ni and Ni_3P at ≤ 800 °C [22–24]. Volume shrinkage during crystallization of amorphous Ni–P coating causes pore formation. Secondly, Ar-3% H_2 gas likely contains ≤ 1 ppm H_2O as impurity with a 4.2×10^{-23} atm. PO_2 calculated by HSC Chemistry 9.0. Hydrogen dissolution in nickel and presence of slight O_2 (< 1 ppm) favors vacancy agglomeration and subsequent growth of pores at the grain boundaries [25].

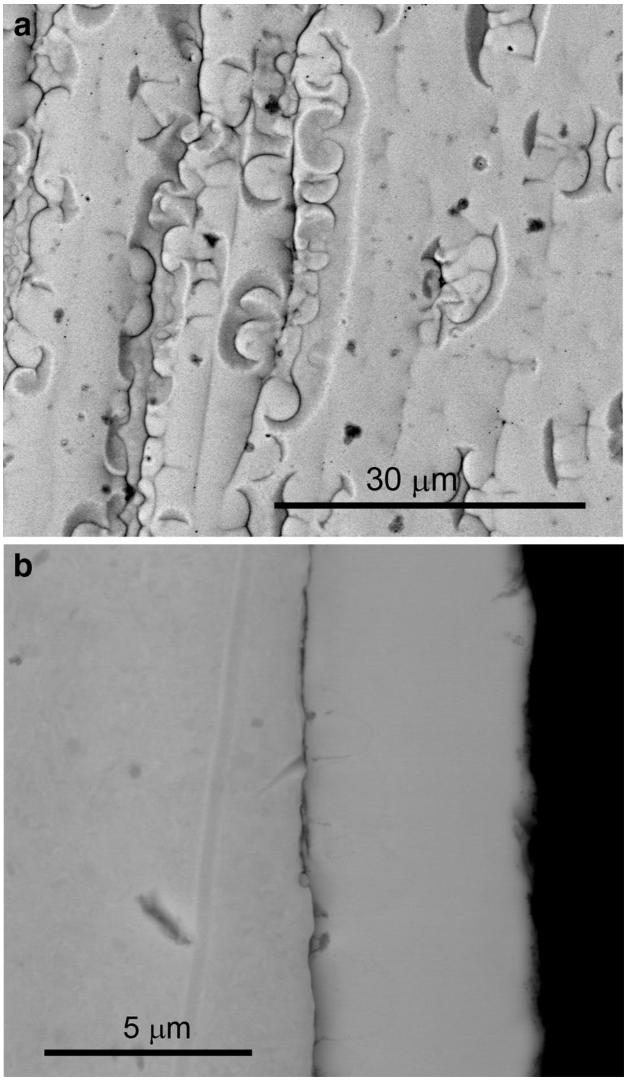

Fig. 2 SEM images of as-received electroless nickel coated AISI 430 alloy: **a** surface, **b** cross-section

Oxygen diffuses through the pores and grain boundaries to form Cr_2O_3 by internal oxidation. Cr_2O_3 is stable up to ~ 10^{-27} atm. PO_2 at 800 °C according to the Ellingham diagram [26].

The cross-sectional SEM image of R-electroless in Fig. 3b shows a 4.63 ± 0.80 μm interaction layer. Dark (arrow marked) phases are observed in the interaction layer and adjacent to the substrate. The interaction layer is nickel and phosphorous rich (5.9 ± 0.2 Fe, 66.0 ± 0.2 Ni, 28.0 ± 0.3 P) while the dark phase is chromium-rich (13.7 ± 2.0 Fe, 24.9 ± 2.4 Cr, 2.4 ± 0.1 Mn, 26.0 ± 2.1 Ni, 40.8 ± 3.0 O).

The EDS line scan profile in Fig. 5 shows that: (1) iron decreases but nickel increases at/near the interaction layer, (2) chromium, manganese, and oxygen are the highest at

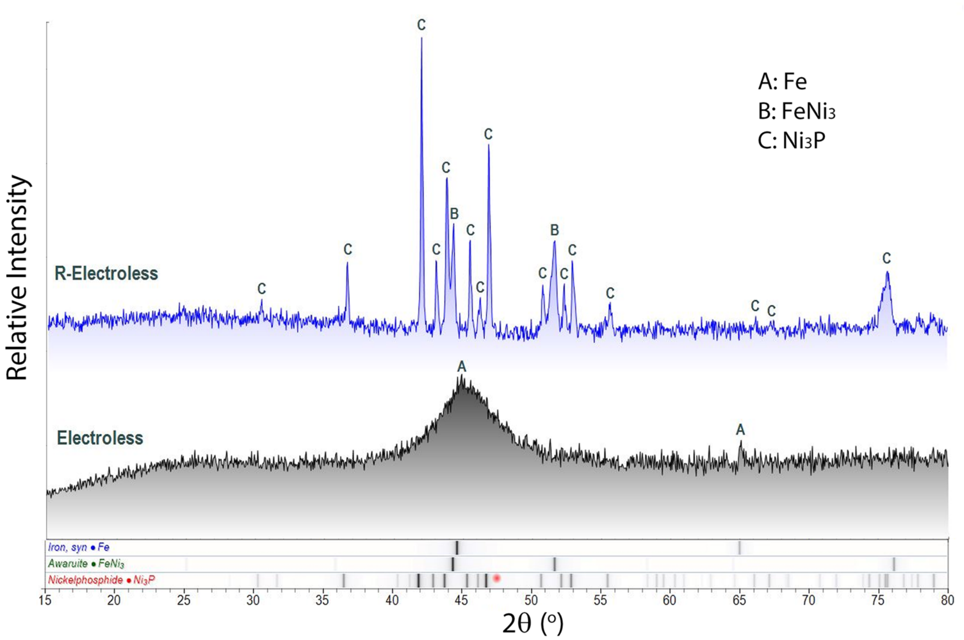

Fig. 3 XRD plots of as-received electroless and R-electroless samples

the dark spots, and (3) nickel diffuses ~ 10 µm into the AISI 430 alloy. The EDS elemental maps in Fig. 6 show that: (1) chromium, manganese, and oxygen overlap at the dark spots, and (2) nickel overlaps with phosphorous at the interaction layer. The EDS analyzes reveal that the dark phases are manganese doped chromium oxide and the interaction layer is the solid solution of nickel and phosphorous. Most of the Ni–Cu topcoat spalled off during metallographic sample preparation leading to non-uniform polishing and iron detection in the top coat.

Ni_3P and $FeNi_3$ intermetallic compounds are detected from XRD analysis in Fig. 3. Ni_3P forms due to the crystallization of amorphous Ni–P coating [22]. $FeNi_3$ forms due to interfusion of nickel and iron. The small quantity of chromium oxide, seen from the SEM image, is beyond the XRD detection limit.

3.2 Oxidation behavior

Figure 7 shows the weight changes due to isothermal oxidation at 800 °C in moisture-saturated air of the electroless and R-electroless samples. The oxidation rate is determined (up to 50 h) by the following equation:

$$\left(\frac{\Delta w}{A}\right)^2 = k_p t \tag{1}$$

where Δw is the weight change due to oxidation, A is the surface area, t is time for isothermal oxidation, k_p is the oxidation rate (mg^2/cm^4 s).

The oxidation rate R-electroless (8.93×10^{-6} mg^2/cm^4 s) is lower than electroless (2.35×10^{-5} mg^2/cm^4 s) sample. The oxidation rate of uncoated AISI 430 alloy (6.08×10^{-5} mg^2/cm^4 s) [27] is higher than that for both the electroless and R-electroless samples.

3.3 Microstructure and XRD analysis

3.3.1 Electroless

The oxide layer of the electroless coating (Fig. 8a) contains equiaxed grains and bright spots (marked as 1) as well. The average size of the equiaxed grains (Fig. 8b) is 5.29 ± 1.44 µm. These grains consist of 28.4 ± 2.3 Fe, 11.6 ± 0.7 Ni, 0.1 ± 0.0 P, and 58.5 ± 3.4 O. The bright grain (arrow marked) shows manganese (1.1 ± 0.1) presence. The bright spots (spot 1) consists of 2.6 ± 0.2 Fe, 0.1 ± 0.0 Cr, 41.5 ± 2.6 Ni, and 55.6 ± 2.7 O. The average size of the equiaxed grains (Fig. 8c) in the bright spots is 1.92 ± 1.40 µm. Pores are observed at the boundaries (marked with dotted boundary in Fig. 8c) between the equiaxed grains in bulk and at the bright spots (1).

Figure 8d shows the cross-sectional microstructure of the oxidized electroless sample. Several distinct features along with pores and cracks are observed in the ~ 65 µm thick oxide layer. Table 2 shows the elemental composition determined from EDS spot analysis. The sublayers in the oxide layer can be described, according to compositional variation, as follows: (i) silicon and oxygen -rich dark spots at the oxide layer/AISI430 interface (marked with gray arrow), (ii) ~ 8 µm thick chromium and oxygen -rich layer 1, (iii) chromium, nickel, and oxygen -rich layer 2, (iii) nickel and oxygen -rich bright spots (spots 4) in a ~ 12 µm thick chromium, iron, and oxygen -rich gray layer 3, (iv) ~ 5 µm

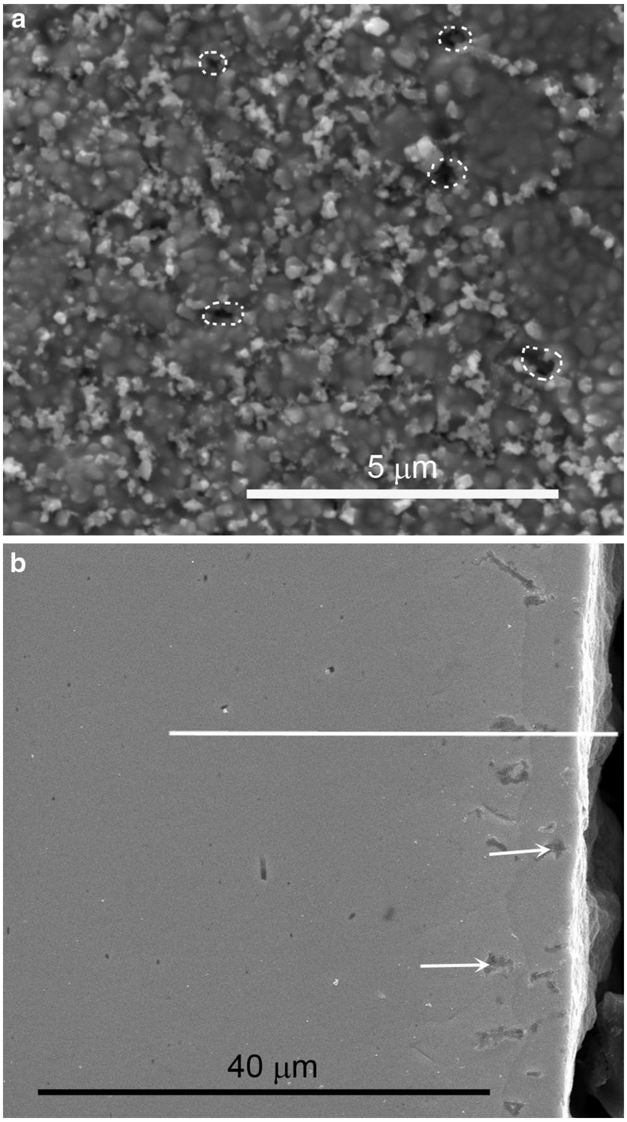

Fig. 4 SEM images of R-electroless sample: **a** surface, **b** cross-section. Solid horizontal line in b corresponds to the EDS line scan in Fig. 5

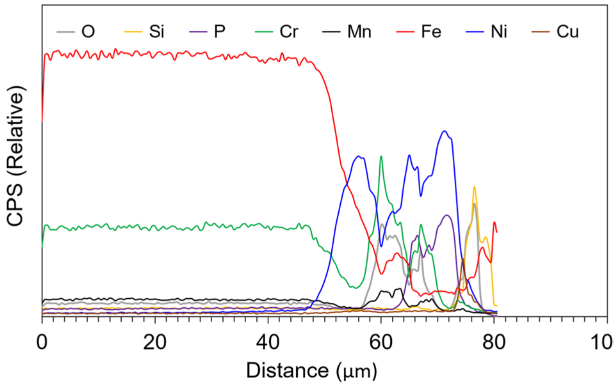

Fig. 5 EDS line scan profile of R-electroless cross-section

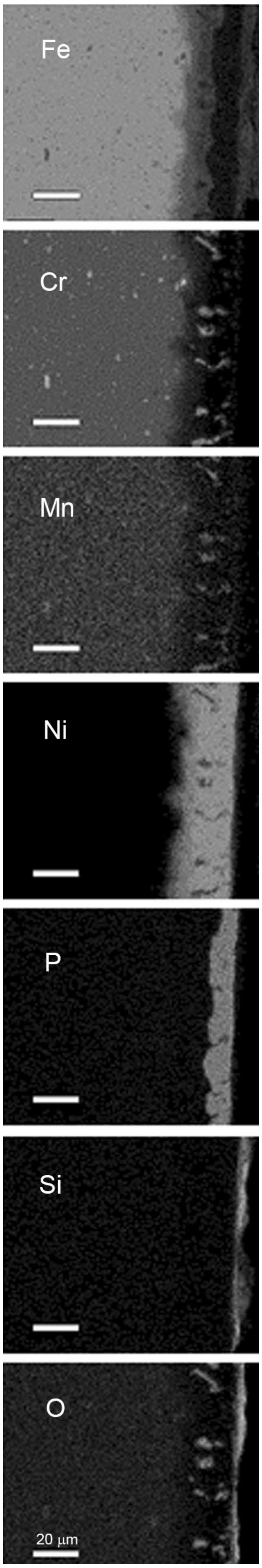

Fig. 6 EDS elemental maps of R-electroless cross-section

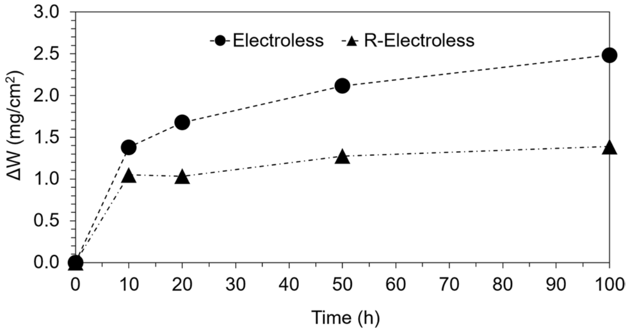

Fig. 7 Weight change versus time for oxidation of the electroless and R-electroless samples at 800 °C in moisture-saturated air

thick phosphorous, iron, and oxygen -rich dark layer 5, (v) ~ 17 μm iron, nickel, and oxygen -rich bright layer 6, (vi) ~ 10 μm thick iron and oxygen -rich gray layer 7, and outermost iron, nickel and oxygen -rich layer 8 of ~ 6 μm thickness with scattered bright phases (marked with white arrow).

Figure 9 shows the elemental concentration profile of the oxidized electroless sample. Various compounds in the oxide layer can reasonably be assigned by comparing the spot analysis and line scan profile, and Cr–Fe–O and Fe–Ni–O phase diagrams [28–31]. The partial pressure of oxygen (P_{O_2}) decreases across the oxide layer from the oxide/gas interface to the AISI 430/oxide interface. The assigned compounds in the oxide layer may differ from XRD analysis since the actual PO_2 in these layers is unknown and EDS provides only elemental composition.

Increase in silicon and oxygen concentration at the oxide layer/substrate interface suggests that the dark spots are SiO_2. Similarly, increased chromium and manganese content between the dark spots and layer 1 indicates the presence of Mn-doped Cr_2O_3. Compositional variation is observed in layer 1. Increase in iron content along with decreased chromium is observed in the first

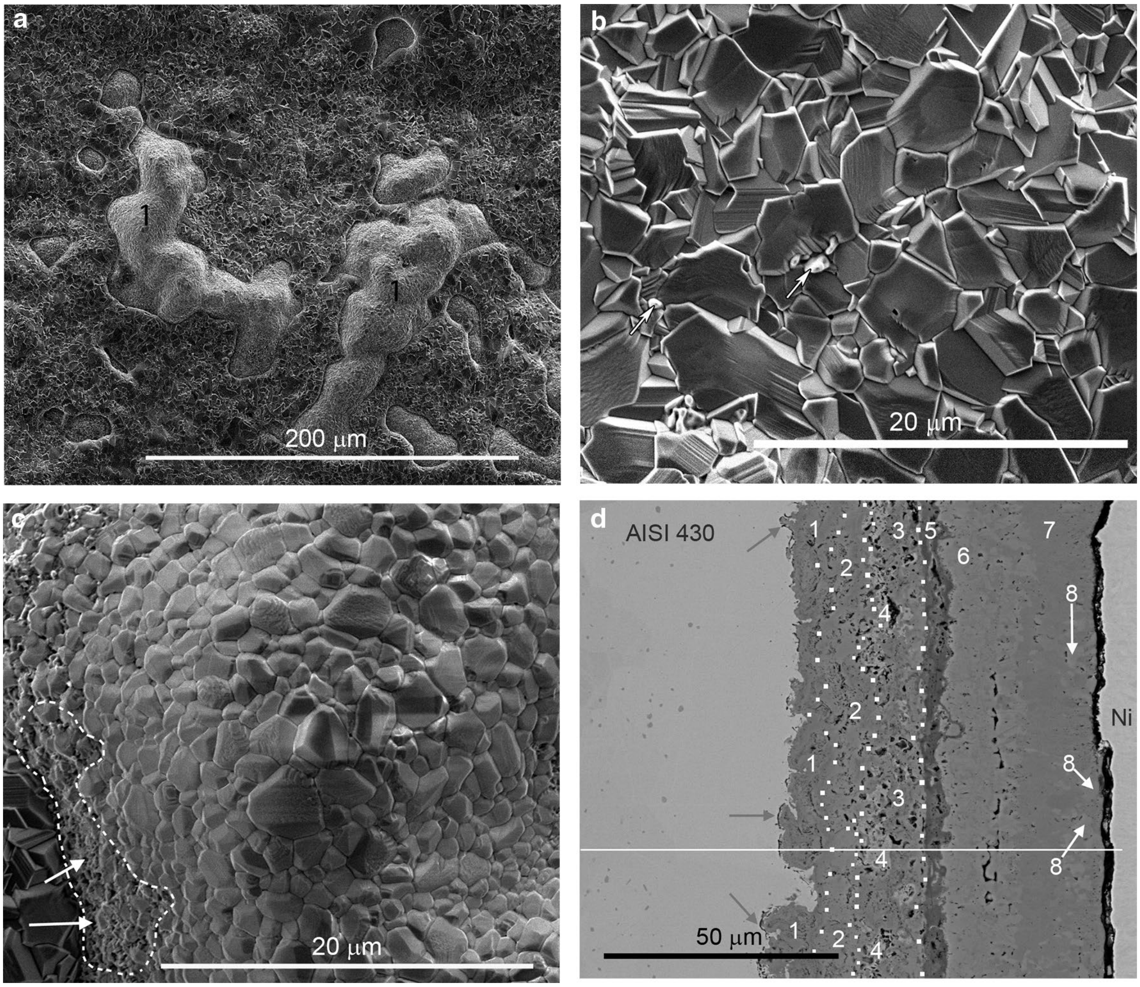

Fig. 8 SEM images of the oxidized electroless sample: **a** surface, **b** higher magnification of surface, **c** higher magnification of bright spots (marked as 1) in a, **d** cross-section. Dotted lines guide the boundaries. Solid horizontal line in d corresponds to the EDS line scan in Fig. 9

Table 2 Elemental composition (at%), determined by EDS spot analysis, across the oxide layer of the oxidized electroless sample

Elements	1	2	3	4	5	6	7	8
O	49.0 ± 1.5	49.4 ± 0.4	53.0 ± 4.6	44.4 ± 0.8	57.8 ± 0.8	62.2 ± 0.6	55.1 ± 0.4	54.8 ± 0.4
Si	0.8 ± 0.3	0.5 ± 0.1	0.5 ± 0.2	0.4 ± 0.2	0.3 ± 0.3	0	0	0
P	0	0.2 ± 0.1	0.8 ± 0.7	0.5 ± 0.3	10.7 ± 2.3	0	0	0
Cr	22.2 ± 4.0	12.3 ± 3.2	18.9 ± 4.9	3.7 ± 1.4	1.0 ± 0.5	0.4 ± 0.2	0	0
Mn	0	0.3 ± 0.2	0.4 ± 0.2	0.1 ± 0.0	0.8 ± 0.7	0	0.3 ± 0.2	0
Fe	27.7 ± 2.3	22.8 ± 2.8	15.6 ± 1.1	4.1 ± 1.5	22.9 ± 3.0	34.3 ± 1.2	44.7 ± 1.7	33.5 ± 1.2
Ni	0.3 ± 0.1	14.5 ± 0.9	10.8 ± 0.8	46.7 ± 2.7	7.6 ± 3.8	13.2 ± 1.3	0	11.7 ± 1.1
Possible compounds	$(Fe,Cr)_{1-x}O$, $FeCr_2O4$	$Fe(Ni,Cr)_2O_4$	$(Fe,Ni)Cr_2O_4$	NiO	Ni_xP	Fe_2NiO_4	Fe_3O_4	Fe_2NiO_4, Fe_3O_4

The numbers indicate corresponding spots in Fig. 8d

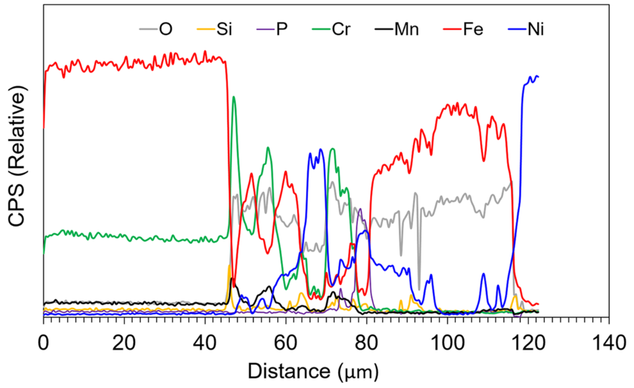

Fig. 9 EDS line scan profile of oxidized electroless sample cross-section

part while iron decreases but chromium and manganese increase in the remaining part. $(Fe,Cr)_{1-x}O$ (halite) and $FeCr_2O_4$ spinel in the first part and $FeCr_2O_4$ spinel in the remaining part are expected according to Cr–Fe–O phase diagram considering the ~ 0.54 mol fraction of iron and low PO_2 ($< 10^{-15}$ bar) in layer 1 [29, 30]. Iron content again increases in layer 2 while chromium content decreases and nickel content increases, indicating halite and $Fe(Ni,Cr)_2O_4$ spinel presence. Chromium content is higher than nickel and iron in layer 3, indicating $(Fe,Ni)Cr_2O_4$ spinel presence. Phosphorous tends to increase in this layer. The bright phases (spot 4) are NiO. Higher concentration of nickel and phosphorus indicates Ni_xP presence in layer 5. Iron content increases and nickel content decreases in layer 6, suggesting Fe_2NiO_4 presence. Negligible nickel content in layer 7 suggests Fe_3O_4 presence. Slight increase in nickel content in layer 8 suggests the presence of Fe_2NiO_4 embedded in a Fe_3O_4 matrix. Considering nickel mole fraction, Fe–Ni–O phase [31] diagram suggests $(Fe,Ni)_3O_4$ spinel and Fe_2O_3 presence in layers 6 and 8. However, the Fe, Ni, and O atomic ratio matches well with Fe_2NiO_4 spinel, consistent with another report [28]. Juxtaposition of the EDS elemental maps in Fig. 10a compliments the EDS line scan profile and spot analyzes. Scattered silicon presence in the oxide layer is noted. Resin impregnation in the pores during metallographic sample preparation is the source of silicon.

Fe_2NiO_4, $Fe_{2.67}O_4$, and Fe_2O_3 compounds are detected from the XRD analysis in Fig. 11. The peak positions corresponds to the diffracted planes for these compounds overlap in the XRD plot. Other plausible compounds, determined from EDS analysis, such as Cr_2O_3, $FeCr_2O_4$, $(Fe,Ni)Cr_2O_4$, Ni_xP, NiO are not detected since these compounds are beyond the X-ray penetration limit of ~ 25 μm depth into the oxide layer [32].

The oxidation of the electroless AISI 430 occurs in multiple steps as discussed below and shown in a schematic diagram in Fig. 12. First, amorphous Ni–P crystallizes above 400 °C into Ni_3P intermetallic compound and nickel oxide (NiO) [12, 22, 33]. NiO, a p-type oxide, grows outward due to Ni^{2+} diffusion through cation vacancies $\left(V_{Ni}''\right)$ in the oxide grain and grain boundaries. At 800 °C and 1 atm. PO_2, grain boundary diffusivity of nickel (~ 2.6×10^{-9} cm^2/s assuming 0.5 nm thick grain boundary) in the oxide is approximately five orders of magnitude higher than the lattice diffusion coefficient (2.1×10^{-14} cm^2/s) [34]. Nickel diffusion through the grain boundaries controls outward growth of NiO associated with voids/pores at Ni_3P/NiO interface [34–36].

Second, oxygen diffuses inward into the AISI 430 substrate through the oxide grains, grain boundaries, and voids/pores and cracks in the oxide. Diffusion of molecular oxygen gas through pores is much higher than oxygen diffusion through grain and grain boundaries. Oxygen diffusion triggers Cr_2O_3 formation by internal oxidation of AISI 430. Cr_2O_3, a p-type oxide, grows externally due to Cr^{3+} diffusion through the cation vacancy (V_{Cr}'''). Cr^{3+} diffuses and dissolves into NiO, and forms $NiCr_2O_4$ spinel. Subsequently, chromium concentration at the AISI 430 adjacent to Cr_2O_3 decreases (~ 14.7 ± 0.4) as confirmed by EDS spot analysis. Mn^{n+} and Fe^{n+} ($n = 2$ or 3) cations diffuse and dissolve into the Cr_2O_3 layer. Diffusivity of the cations in Cr_2O_3 decreases in the order

Fig. 10 EDS elemental maps of oxidized **a** electroless and **b** R-electroless cross-sections

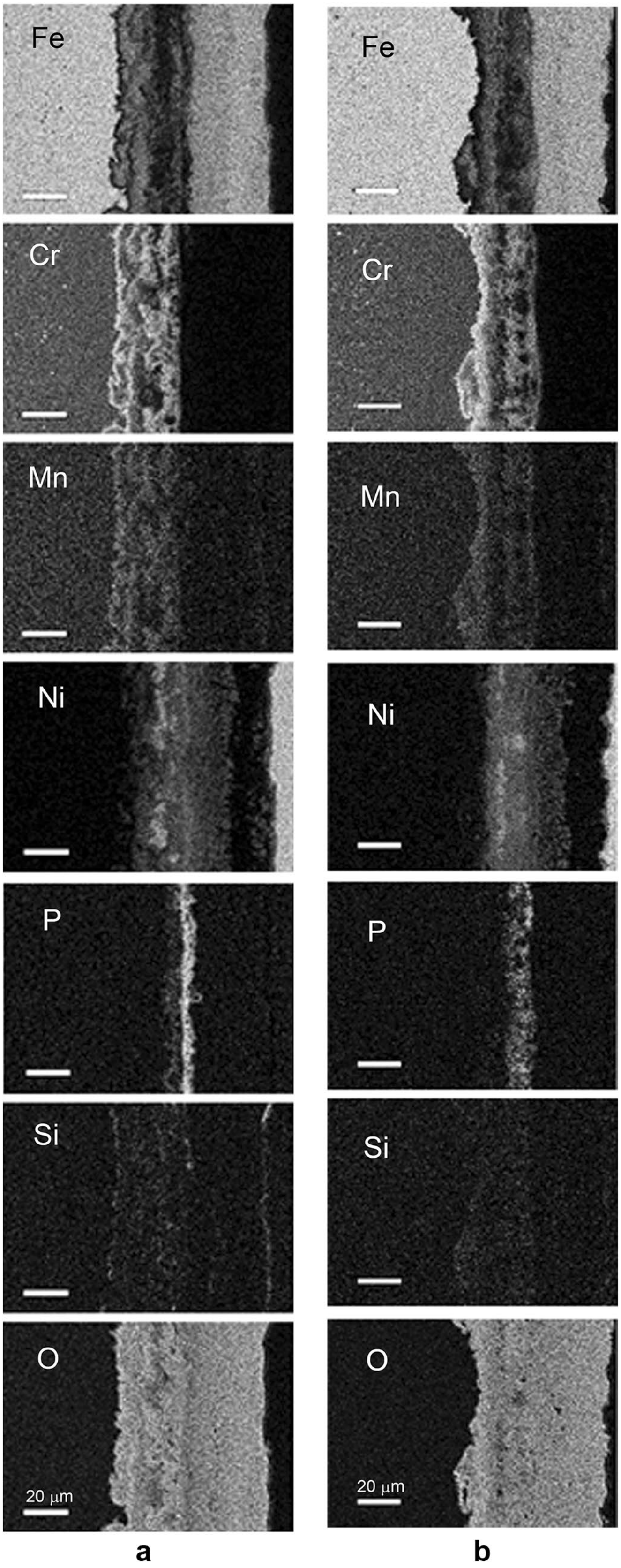

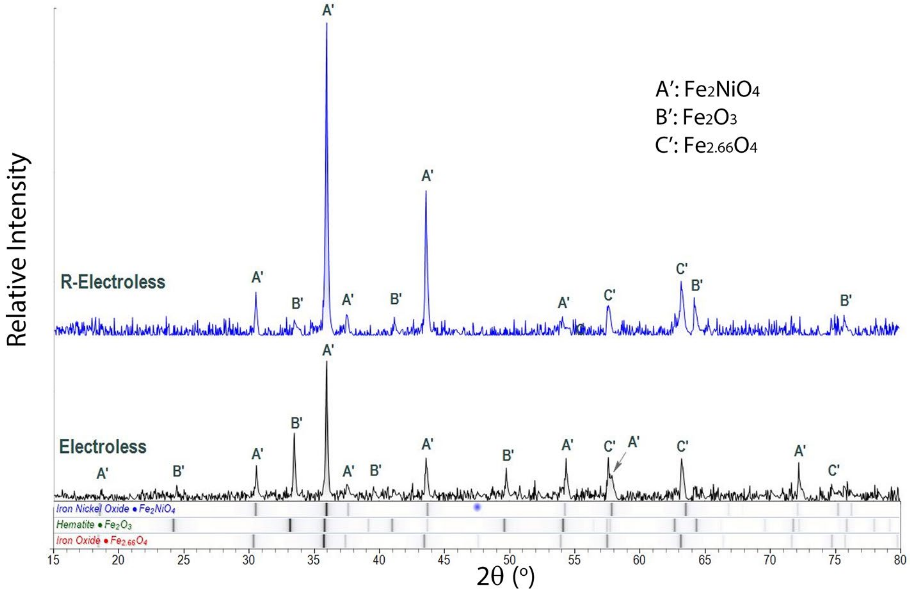

Fig. 11 XRD plots of oxidized electroless and R-electroless samples

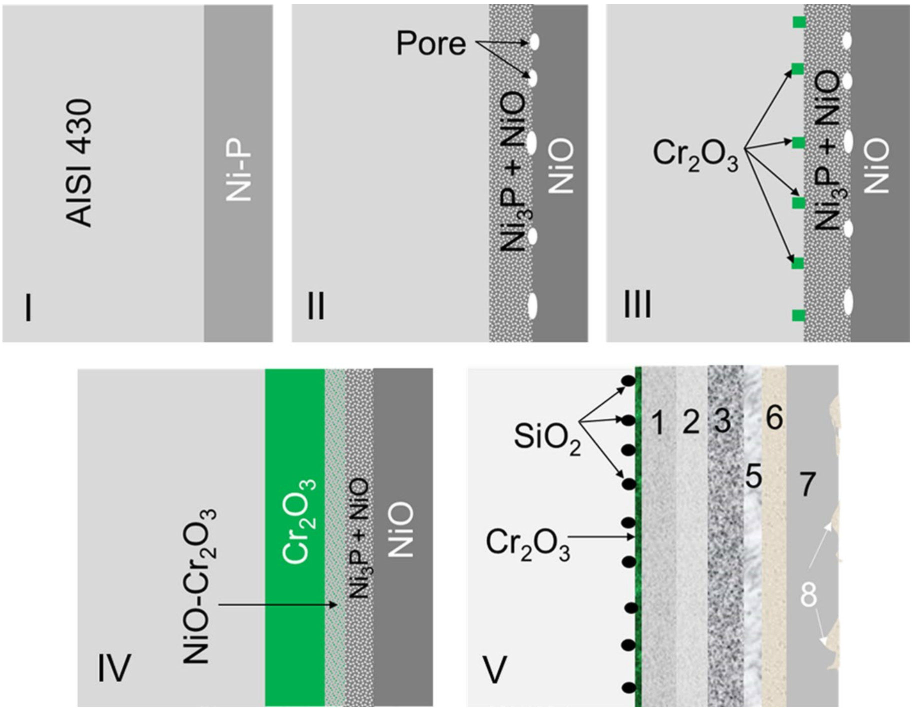

Fig. 12 Schematic diagram to illustrate different oxidation stages (I–V) for electroless sample. See text for detail. Arabic numbers correspond to Fig. 8d and Table 2

of $D_{Cr} < D_{Ni} < D_{Fe} < D_{Mn}$ [37]. Mn^{n+} dissolves into the Cr_2O_3 as supported by overlapping chromium and manganese maps (Fig. 10a). Fe^{n+} continues to diffuse into the Cr_2O_3 due to higher concentration and forms $(Fe,Cr)_{1-x}O$ and $FeCr_2O_4$ phases, suggesting the absence of $MnCr_2O_4$ spinel since its presence should retard interdiffusion of ions. Simultaneously, Ni^{2+} also diffuses towards the substrate due to chemical potential gradient of nickel and dissolves into the $FeCr_2O_4$ spinel. As a result, $(Fe,Cr)_{1-x}O$ and $(Fe,Ni)Cr_2O_4$ are formed in layer 2. Both Fe^{n+} and Cr^{3+} dissolve into NiO lattice and form $(Fe,Ni)Cr_2O_4$ or $(Fe,Ni,Cr)_xO_4$ spinel in layer 3.

Iron diffuses through Ni–P layer into NiO, but manganese and chromium diffusion is not observed. Approximate 1:1 Ni and P atomic ratio in the layer 5 (as seen from EDS spot analysis) suggests NiP presence, which exists above 800 °C according to Ni–P phase diagram [38]. Iron diffusion into the Ni–P layer likely promotes NiP formation at ≤ 800 °C, similar to the observation for Ni–P-Re crystallization. Decomposition of Ni_3P into $Ni_{12}P_5$, Ni_2P and NiO at

> 500 °C has been reported [22]. Overlapping iron, nickel, and phosphorous maps indicates the presence of Fe_xP compound. Oxygen presence in the layer 5 suggests also the presence of oxide phases such as Fe_2O_3 and (Fe,Ni)O [31]. Lower phosphorus content in the oxide layer than the as-received sample is noted. Sublimation of P_2O_5 during Ni_3P oxidation [39] attributes to lower the phosphorous content, supported by pores in layer 5.

Third, Fe^{n+} continues to diffuse through the cation vacancies $\left(V_{Ni}''\right)$ in NiO grains and grain boundaries, dissolves into the NiO lattice, and forms Fe_2NiO_4 spinel. Diffusivity of iron in NiO is higher than the self-diffusivity of nickel [40], leading to iron oxide formation. Fe_3O_4, a p-type oxide, prefers to form first because of its higher stability than FeO and Fe_2O_3 [41]. Fe^{2+} diffusion into the Fe_3O_4 causes $Fe_{2.94}O_3$ and Fe_2O_3 formation [42]. Another study in literature reports $(Fe,Ni)_3O_4$ and Fe_2O_3 formation [19]. However, Fe_2NiO_4 is detected by XRD, consistent with another study [28]. In parallel, nickel also diffuses inward due to chemical potential gradient across the oxide layer. Nickel does not diffuse beyond layer 2 since D_{Cr} in NiO > D_{Ni} in Cr_2O_3 [37, 40]. Difference in diffusivity of the cations generate vacancies, which coalesce into voids. Difference in the thermal expansion co-efficient between the compounds also generate pores and voids to accommodate thermal stress [42]. For instance, the thermal expansion coefficient of $NiFe_2O_4$, Fe_2O_3 and Fe_3O_4 are, respectively, $\sim 10.8 \times 10^{-6}$/ °C [43], $\sim 12.0 \times 10^{-6}$/ °C, and 15.0×10^{-6}/ °C [44].

Fourth, AISI 430 alloy adjacent to the oxide layer is chromium deficient (79.2 ± 1.1 Fe, 14.7 ± 0.4 Cr, 0.5 ± 0.1 Mn, 0.5 ± 0.2 Ni, 0.2 ± 0.1 P, 0.3 ± 0.2 Si, 4.0 ± 0.3 O). SiO_2 forms by internal oxidation due to inward oxygen diffusion and chromium deficiency at the AISI 430 alloy. SiO_2 layer acts as a barrier for elemental interdiffusion across the AISI 430/oxide layer interface and prevents further oxidation [42].

3.3.2 R-electroless

The oxide layer of the R-electroless sample (Fig. 13a) contains grains (31.3 ± 0.0 Fe, 0.5 ± 0.1 Mn, 10.2 ± 1.0 Ni, and 58.2 ± 1.2 O), and platelets (30.2 ± 2.8 Fe, 0.5 ± 0.1 Mn, 3.2 ± 0.8 Ni, and 66.1 ± 2.2 O), and bright spot (marked with arrow in Fig. 13b) at grain boundaries (26.9 ± 2.3 Fe, 0.5 ± 0.1 Mn, 6.4 ± 0.9 Ni, and 66.3 ± 2.7 O). Pores are observed at the grain boundaries for two plausible reasons. Cr_2O_3 at the grain boundaries (bright spots in Fig. 4a) in unoxidized R-electoless AISI 430 evaporates as CrO_3 and $CrO_2(OH)_2$ species [45], supported by the absence of chromium in EDS spot analysis. Molecular oxygen at the voids/pores preferes diffusion of cations from the $FeNi_3$ intermetallic towards the grain boundaries to form oxides, forming voids at the metal/oxide interface. The voids coalease into large pores to reduce surface energy.

Figure 13c, d show the cross-sectional microstructure of the oxidized R-electroless sample. Several distinct features along with pores and cracks are observed in the ~ 65 µm thick oxide layer. Table 3 shows the elemental composition determined from EDS spot analysis. The sublayers in the oxide layer can be described as follows: (i) silicon and oxygen-rich sporadic dark spots (marked by gray arrow), at the oxide layer/AISI 430 interface (ii) chromium and oxygen-rich thin layer 1 (marked by dotted boundary), (iii) chromium, iron, and oxygen- rich layer 2, (iii) ~ 8 µm thick iron, chromium, nickel and oxygen -rich bright layer 3, (iv) ~ 12 µm thick layer 4 consisting of phosphorous and oxygen -rich gray phases and iron, chromium, nickel and oxygen -rich bright phases, (v) ~ 15 µm thick layer 5 consisting of iron, nickel, and oxygen-rich bright phases in an iron and oxygen-rich gray phase, (vi) iron and oxygen-rich layer 6 of ~ 17 µm thickness, and (vii) an outermost thin layer 7 of iron, nickel and oxygen -rich.

Figure 14 shows the elemental concentration profile of the oxidized R-electroless samples. The compounds in the oxide layer can be assigned by the similar approach used for the oxidized electroless sample. Increase in silicon and oxygen concentration at the oxide layer/substrate interface suggests that the dark spots are SiO_2. Similarly, increase in manganese and chromium suggests the presence of manganese doped Cr_2O_3 in the layer 1. Other possible compounds in the oxide layers are listed in the Table 3. Juxtaposition of the EDS elemental maps in Fig. 10b compliment the plausible phases identified from EDS spot analysis and line scan profile.

Fe_2NiO_4, $Fe_{2.67}O_4$, and Fe_2O_3 compounds are detected from the XRD analysis. The peak positions corresponds to the diffracted planes for these compounds overlap in the XRD plot. Other compounds such as Cr_2O_3, $FeCr_2O_4$, $(Fe,Cr)_{1-x}O$, $(Fe,Ni)Cr_2O_4$, (Ni,Fe)O are not detected since these compounds are beyond the X-ray penetration limit of ~ 25 µm depth into the oxide layer.

There are similarities and distinct differences between the oxide layers of the electroless and R-electroless samples. The sublayers between the AISI 430 and the phosphorous containing layer are almost same for both the samples. Iron oxide layer is also overserved for both the samples. The phosphorous containing layer (layer 4 in Fig. 13c) is thicker and more porous for the R-electroless sample compared to the electroless sample (layer 5 in Fig. 8d). Ni_xP and $FeCr_2O_4$ phases are likely present as seen from the overlapping of nickel and phosphorous maps and elemental iron and chromium maps (Fig. 10b). $NiFe_2O_4$ spinel embedded in iron oxide is observed in layer 5 of R-electroless sample unlike a continuous $NiFe_2O_4$ spinel in layer 6 of electroless sample. In the outermost layer, $NiFe_2O_4$

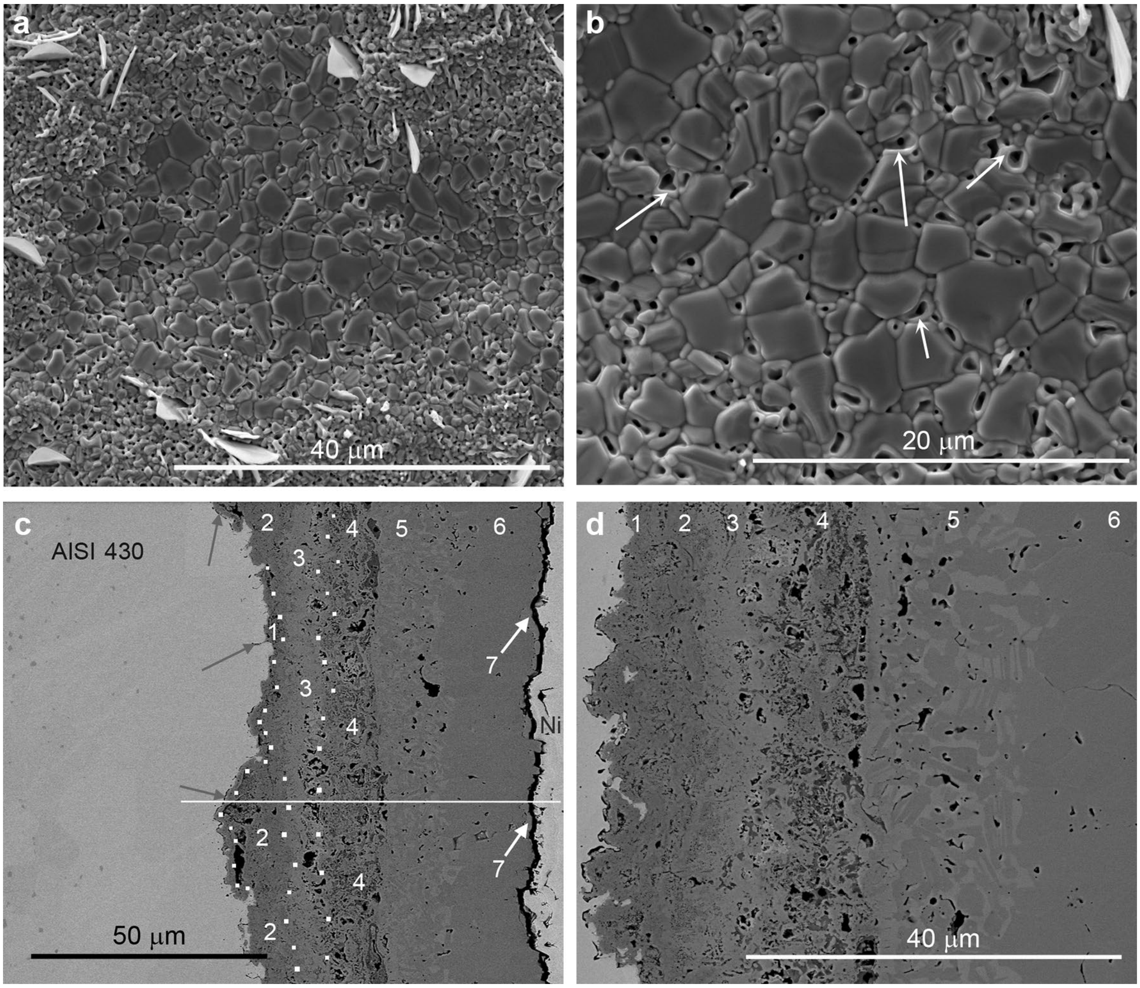

Fig. 13 SEM images of the oxidized R-electroless sample: **a** surface, **b** higher magnification of surface image, **c** cross-section, **d** higher magnification of cross-sectional image. Solid horizontal line in c corresponds to the EDS line scan in Fig. 14

Table 3 Elemental composition (at%), determined by EDS spot analysis, across the oxide layer of the oxidized R-electroless sample

Elements	1	2	3	4 (gray)	4 (bright)	5	6	7
O	41.0 ± 1.9	39.8 ± 1.3	42.8 ± 0.8	49.3 ± 5.2	45.3 ± 2.1	52.4 ± 0.8	52.5 ± 1.6	58.7 ± 3.4
Si	2.0 ± 0.4	2.7 ± 1.5	1.2 ± 0.1	1.1	1.5 ± 0.4	0.7	0	1.1 ± 0.1
P	0	0	0.9	11.6 ± 5.1	3.3 ± 1.8	0	0	0
Cr	47.6 ± 4.4	29.6 ± 15.0	15.3 ± 2.6	8.8 ± 9.0	18.7 ± 6.4	0.8 ± 0.4	1.9 ± 1.8	0
Mn	1.2 ± 0.2	0	0	0.4 ± 0.2	0.1 ± 0.1	0.3 ± 0.3	0	2.0 ± 0.1
Fe	8.7 ± 4.4	26.9 ± 14.8	24.9 ± 2.4	13.4 ± 1.5	15.6 ± 5.5	36.4 ± 2.9	43.3 ± 1.1	25.8 ± 1.4
Ni	0.5 ± 0.4	1.2 ± 0.6	16.3 ± 0.8	15.7 ± 4.1	16.1 ± 1.1	10.2 ± 2.5	2.3 ± 1.1	13.1 ± 5.1
Possible compounds	Cr_2O_3	$(Fe,Cr)_{1-x}O$, $FeCr_2O_4$	$(Fe,Ni)Cr_2O_4$	Ni_xP, $NiCr_2O_4$, $FeCr_2O_4$	Fe_2NiO_4, (Ni, Fe)O	Fe_2NiO_4, Fe_3O_4	Fe_3O_4	Fe_2NiO_4, Fe_3O_4

The numbers indicate corresponding spots in Fig. 13c

spinel is distributed in Fe_2O_3 for the electroless sample while an almost continuous spinel layer is observed for the R-electroless sample.

The oxidation of R-electroless sample is discussed in terms of the oxidation of $FeNi_3$ intermetallic [46] and Ni_3P layer and the plausible steps are shown in a schematic

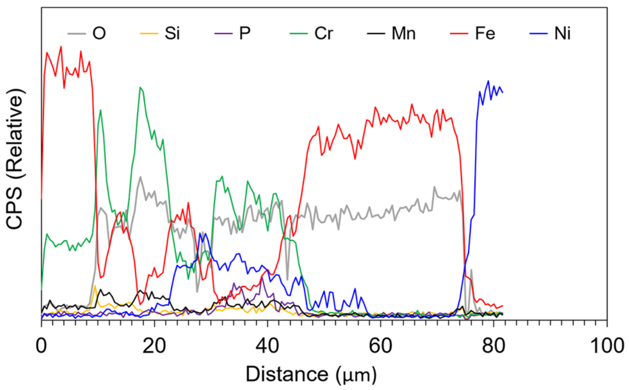

Fig. 14 EDS line scan profile of oxidized R-electroless cross-section

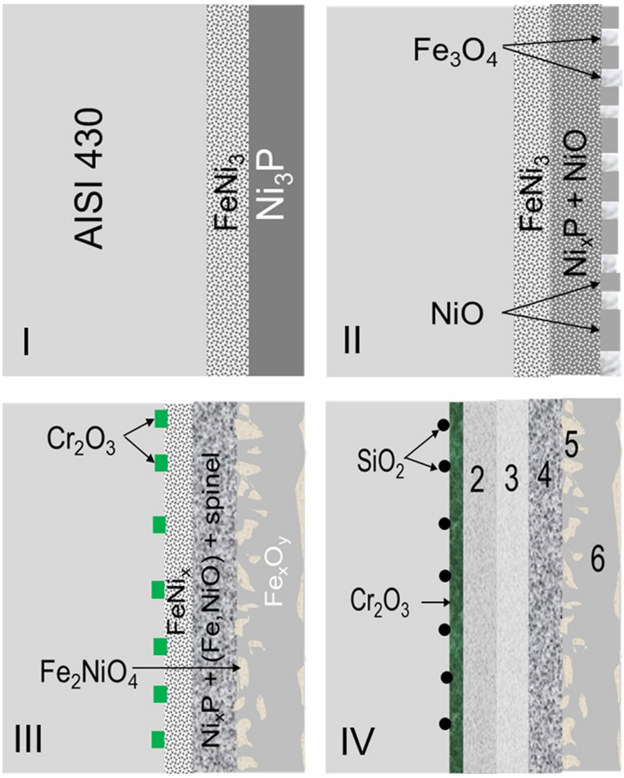

Fig. 15 Schematic diagram to illustrate different oxidation stages (I–IV) for R-electroless sample. See text for detail. Arabic numbers correspond to Fig. 13c and Table 3

diagram in Fig. 15. Fe is also detected in Ni_3P layer. Fe_3O_4 forms first due to its higher thermodynamic stability than NiO [41, 42]. However, iron content in Ni_3P layer is not sufficient to form a continuous Fe_3O_4 oxide layer. Ni_3P oxidizes into Ni_xP phases and NiO [22]. A mixed NiO and Fe_3O_4 layer forms accompanied with pores at the Ni_3P and oxide layer interface.

Iron from $FeNi_3$ intermetallic diffuses through Ni_xP, NiO, and Fe_3O_4 [16–19], dissolves into these oxides, and forms Fe_2NiO_4 and $Fe_{2.67}O_4$. Further diffusion of iron through Fe_2NiO_4 and $Fe_{2.67}O_4$ continues to form Fe_2O_3.

$FeNi_3$ becomes iron deficient and NiO formation starts. NiO forms solid solution with Fe_3O_4 and also forms $NiFe_2O_4$ spinel. Iron and nickel both diffuses through the Fe_3O_4 and $NiFe_2O_4$ spinel but diffusivity of iron is higher than nickel [37]. So, iron oxide ($Fe_{2.67}O_4$ and/or Fe_2O_3) grows outward.

Similar to the electroless sample, Cr_2O_3 forms due to internal oxidation of AISI 430 by inward oxygen diffusion as discussed in the previous section. $FeCr_2O_4$, $(Fe,Cr)_{1-x}O$, $(Fe,Ni)Cr_2O_4$, (Ni,Fe)O compounds form by the similar mechanisms as discussed for the electroless sample.

The present study is limited to isothermal oxidation of the electroless and R-electroless AISI 430 alloys at 800 °C for 100 h dwell time. Microstructure and elemental compositional analysis, supported by literature reports, provides substantial information on the oxidation behavior. Further investigation is required at varying temperatures and isothermal dwell times for a comprehensive understanding of the oxidation kinetics of Ni–P coated AISI 430 alloy.

4 Conclusion

The oxidation behavior of electroless Ni–P coated AISI 430 and pre-reduced Ni–P coated AISI 430 was investigated at 800 °C in moisture-saturated (~ 3% H_2O) air by microstructural and compositional analysis. The oxidation rate pre-reduced Ni–P coated AISI 430 is lower than electroless sample. Ni–P coating crystallization and oxidation initiates the oxidation for the electroless sample while Ni_3P and $FeNi_3$ intermetallic compounds initiates the oxidation of the pre-reduced sample. Multilayered oxide scale with mixed oxide and spinel phases is formed by diffusion controlled oxidation mechanism in both the electroless and pre-reduced Ni–P coated AISI 430.

Acknowledgements US Department of Energy funded the research under the Grant number: DE-FE 0023385. One author (MK) is grateful to NASA Alabama Space Grant Consortium (ASGC) Graduate Fellowship (Number: NNX15AJ18H) program. The authors thank Dr. Prabhakar Singh, University of Connecticut for helpful discussion.

Compliance with ethical standards

Conflicts of interest The authors declare, to the best of their knowledge, no conflict of interest in the manuscript.

References

1. Sudagar J, Lian J, Sha W (2013) Electroless nickel, alloy, composite and nano coatings—a critical review. J Alloys Compd 571:183–204

2. Kundu S, Das SK, Sahoo P (2014) Properties of electroless nickel at elevated temperature—a review. Proc Eng 97:1698–1706
3. Lee CK (2008) Corrosion and wear-corrosion resistance properties of electroless Ni–P coatings on GFRP composite in wind turbine blades. Surf Coat Technol 202:4868–4874
4. Lee CK (2009) Structure, electrochemical and wear-corrosion properties of electroless nickel–phosphorus deposition on CFRP composites. Mater Chem Phys 114:125–133
5. Cheng YH, Zou Y, Cheng L, Liu W (2008) Effect of the microstructure on the anti-fouling property of the electroless Ni–P coating. Mater Lett 62:4283–4285
6. Rani RU, Sharma AK, Minu C, Poornima G, Tejaswi S (2010) Studies on black electroless nickel coatings on titanium alloys for spacecraft thermal control applications. J Appl Electrochem 40:333–339
7. Mallory GO (1990) The fundamental aspects of electroless nickel plating. Electroless Plating: Fundamentals and Applications. Cambridge University Press, Cambridge, pp 1–57
8. Parkinson R (1997) Properties and applications of electroless nickel. Nickel Development Institute Publication, 33
9. Jordanov NB (2019) Electrodeposition of amorphous Ni–P layers, thermal treatment and corrosion behavior. Trans IMF 97:115–120
10. Yan M, Ying HG, Ma TY (2008) Improved microhardness and wear resistance of the as-deposited electroless Ni–P coating. Surf Coat Technol 202:5909–5913
11. Sahoo P, Das SK (2011) Tribology of electroless nickel coatings—a review. Mater Design 32:1760–1775
12. Keong KG, Sha W (2002) Crystallisation and phase transformation behaviour of electroless nickel-phosphorus deposits and their engineering properties. Surf Eng 18:329–343
13. Schwartz M, Mallory GO (1976) Effect of heat-treatments on magnetic properties of electroless nickel alloys. J Electrochem Sci 123:606–614
14. Shong WJ, Liu CK, Yang P (2012) Effects of electroless nickel plating on 441 stainless steel as SOFC interconnect. Mater Chem Phys 134:670–676
15. Glazoff MV, Rashkeev SN, Herring JS (2014) Controlling chromium vaporization from interconnects with nickel coatings in solid oxide devices. Int J Hydrog Energy 39:15031–15038
16. Lin KL, Lai PJ (1990) Interdiffusion of the electroless Ni-P deposit with the steel Substrate. J Electrochem Soc 137:1509–1513
17. Weiss Z (1992) High-temperature oxidation of iron covered by electroless Ni-P coating: a GDOS depth profiling study. Surf Inter Anal 8:691–694
18. Lo PH, Tsai WT, Lee J, Hung MP (1993) The study of interdiffusion phenomena of Ni-P/steel interface. Script Metal Mater 29:37–42
19. Eraslan S, Ürgen M (2015) Oxidation behavior of electroless Ni–P, Ni–B and Ni–W–B coatings deposited on steel substrates. Surf Coat Technol 265:46–52
20. Mahapatra MK, Lu K (2011) Effect of atmosphere on interconnect-seal glass interaction for solid oxide fuel/electrolyzer cells. J Am Ceram Soc 94:875–885
21. Goldstein J, Newbury D, Joy D, Lyman C, Echlin P, Lifshin E, Sawyer L, Michael J (2007) Scanning electron microscopy and X-ray microanalysis, 3rd edn. Springer, New York
22. Pfeiffer H, Tancret F, Brousse T (2005) Synthesis, characterization and thermal stability of Ni_3P coatings on nickel. Mater Chem Phys 92:534–539
23. Wojewoda-Budk J, Wierzbicka-Miernik A, Litynska-Dobrzynska L, Szczerba MJ, Mordarski G, Mosiałek M, Huber Z, Zieba P (2016) Microstructure characteristics and phase transformations of the Ni-P and Ni-P-Re electroless deposited coatings after heat treatment. Electrochim Acta 209:183–191
24. Keong KG, Sha W, Malinov S (2002) Crystallization kinetics and phase transformation behaviour of electroless nickel–phosphorus deposits with high phosphorus content. J Alloys Compd 334:192–199
25. Connetable D, David M, Prillieux A, Young D, Monceau D (2017) Impact of the clusterization on the solubility of oxygen and vacancy concentration in nickel: a multi-scale approach. J Alloys Compd 708:1063–1072
26. Young J (2008) Enabling theory. In: Young DJ (ed) High temperature oxidation and corrosion of metals. Elsevier, Oxford, pp 31–84
27. King MK, Mahapatra MK (unpublished work)
28. Hansson AN, Mogensen M, Linderoth S, Somers MAJ (2003) Inter-diffusion between NiO coating and the oxide scale on Fe-22Cr alloy. J Corr Sci Eng 6:H017
29. Taylor JR, Dinsdale AT (1983) A thermodynamic assessment of the Cr-Fe-O system. Z Metallkd 84:335–345
30. Pelton AD, Schmalzr H, Sticher J (1979) Computer-assisted analysis and calculation of phase diagrams of the Fe-Cr-O, Fe-Ni-O and Cr-Ni-O systems. J Phys Chem Solids 40:1103–1122
31. Rhamdhani MA, Hayes PC, Jak E (2008) Subsolidus phase equilibria of the Fe-Ni-O System. Metal Mater Trans B 39B:690–701
32. Klug HP, Alexander LE (1974) X-ray diffraction procedures for polycrystalline and amorphous materials, 2nd edn. Wiley, New York
33. Tan YY, Sun DB, Yang B, Gong Y, Yan S, Du R, Guo HL, Chen W, Xing XQ, Mo G, Chen ZJ, Cai Q, Wu ZH, Yu HY (2013) In-situ crystallization study of amorphous Ni-P nanoparticles with high P content. In: Proc 13th IEEE Int Conf Nanotech, Beijing, China, August 5–8, 2013, pp 618–621
34. Atkinson A (1982) A quantitative demonstration of the grain boundary diffusion mechanism for the oxidation of metals. Philos Mag A 45A:823–833
35. Atkinson A, Taylor RI (1978) The self-diffusion of Ni in NiO and its relevance to the oxidation of Ni. J Mater Sci 3:427–432
36. Nakamura R, Lee JG, Mori H, Nakajima H (2008) Oxidation behaviour of Ni nanoparticles and formation process of hollow NiO. Philos Mag 88:257–264
37. Lobnig RE (1992) Diffusion of cations in chromia layers grown on iron-base alloys. Oxid Metals 37:81–93
38. Okamoto H (2010) Ni-P (Nickel-phosphorus). JPEDAV 31:200–201
39. Pai ST, Marton JP (1973) The composition of oxides formed on electroless Ni–P deposits. J Electrochem Soc 120:1280–1281
40. Monty C (1983) Diffusion in stoichiometric and non-stoichiometric cubic oxides. Rad Eff 74:29–55
41. Brandes EA, Brook GB (1998) Smithells metals reference book, 7th edn. Butterworth Heinemann, Oxford
42. Birks N, Meier GM, Pettit FS (2006) Introduction to high temperature oxidation of metals, 2nd edn. Cambridge University Press, Cambridge
43. Shaigan N (2010) A review of recent progress in coatings, surface modifications and alloy developments for solid oxide fuel cell ferritic stainless steel interconnects. J Power Sources 195:1529–1542
44. Takeda M, Onishi T, Nakakubo S, Fujimoto S (2009) Physical properties of iron-oxide scales on Si-containing steels at high temperature. Mater Trans 50:2242–2246
45. Ebbinghaus BB (1993) Thermodynamics of gas phase chromium species: the chromium oxides, the chromium oxyhydroxides, and volatility calculations in waste incineration processes. Comb Flame 93:119–137
46. Meier GH, Pettit ES (1992) The oxidation behavior of intermetallic compounds. Mater Sci Eng Al 53:548–560